INTERNATIONAL JOURNAL FOR NUMERICAL METHODS IN BIOMEDICAL ENGINEERING
Int. J. Numer. Meth. Biomed. Engng. 2013; **29**:887–904
Published online 27 June 2012 in Wiley Online Library (wileyonlinelibrary.com). DOI: 10.1002/cnm.2498

COMPUTATIONAL METHODS FOR BIOMEDICAL IMAGE PROCESSING AND ANALYSIS

Automatic MRI 2D brain segmentation using graph searching technique

Valentina Pedoia*,† and Elisabetta Binaghi

Dipartimento di Scienze Teoriche e Applicate, Università degli Studi dell'Insubria, Via Mazzini 5 Varese, Italy

SUMMARY

Accurate and efficient segmentation of the whole brain in magnetic resonance (MR) images is a key task in many neuroscience and medical studies either because the whole brain is the final anatomical structure of interest or because the automatic extraction facilitates further analysis. The problem of segmenting brain MRI images has been extensively addressed by many researchers. Despite the relevant achievements obtained, automated segmentation of brain MRI imagery is still a challenging problem whose solution has to cope with critical aspects such as anatomical variability and pathological deformation. In the present paper, we describe and experimentally evaluate a method for segmenting brain from MRI images basing on two-dimensional graph searching principles for border detection. The segmentation of the whole brain over the entire volume is accomplished slice by slice, automatically detecting frames including eyes. The method is fully automatic and easily reproducible by computing the internal main parameters directly from the image data. The segmentation procedure is conceived as a tool of general applicability, although design requirements are especially commensurate with the accuracy required in clinical tasks such as surgical planning and post-surgical assessment. Several experiments were performed to assess the performance of the algorithm on a varied set of MRI images obtaining good results in terms of accuracy and stability. Copyright © 2012 John Wiley & Sons, Ltd.

Received 28 December 2011; Revised 12 March 2012; Accepted 20 May 2012

KEY WORDS: MRI segmentation; brain segmentation; boundary detection; graph optimization

1. INTRODUCTION

Magnetic resonance imaging (MRI) is one of the most recently developed forms of neuroimaging and has quickly become a popular tool for obtaining images with high contrast of brain tissues. By using different acquisition parameter settings, MRI scanning allows to obtain different images of the same body where various types of tissues and neuropathology can be differentiated [1, 2].

Accurate and efficient segmentation of the whole brain in magnetic resonance (MR) images is a key task in many neuroscience and medical studies either because the whole brain is the final anatomical structure of interest or because the automatic extraction facilitates further analysis [3, 4]. Whole brain segmentation is a task available in software such as Brain Visa [5], FSL [6] and Brainsuite [7]; however, in most cases, they give poor results especially in case of tumors located on the border of the brain [4].

The problem of segmenting all or part of the brain in MRI imagery continues to be investigated giving rise to a variety of approaches attempting to satisfy the high accuracy demand in diversified

*Correspondence to: Valentina Pedoia, Collegue of Dipartimento di Scienze Teoriche e Applicate Università degli Studi dell'Insubria, Via Mazzini 5 Varese, Italy.

†E-mail: valentina.pedoia@uninsubria.it

clinical and neuroimaging application [1–4]. The rationale behind this effort is to improve upon existing early methods suffering from incorrect detection because of noise, difficulties in assigning threshold in the edge image and over and under estimation. The proposed solutions make use of a single, gray scale two-dimensional (2D) or three-dimensional (3D) image or multiple MR images with different gray scale contrast [1]. Focusing on whole brain segmentation from gray scale images, the early most intuitive approach proposed is automatic thresholding. The application of this approach to MR brain image segmentation includes works based on iterative, knowledge guided thresholding [8, 9] and histogram analysis [10] complemented in some cases with image processing techniques such as morphological filtering [11]. The solutions proposed suffer in general from the difficulty in setting threshold values and present strong limitations in the presence of inhomogeneity, image artifact and anatomical variability. The Region Growing approach extends thresholding by combining it with connectivity. Methods within this approach need an operator for manual setting of seed for each region, and their results depend on the heuristic assessment of thresholding for homogeneity [12, 13]. As a consequence, suitable accuracy is achieved only detecting the contour in slices where the brain is one homogeneous region without pathological alterations and inhomogeneity.

Supervised statistical pattern recognition approaches are proposed in MR image segmentation to circumvent the problem of explicitly and analytically describing the specific segmentation procedure and related parameters, lying, to a learning stage, the charge of inducing the classifier from supervised data available. Parametric and nonparametric methods are proposed showing a competitive behavior in reducing the effect of radio frequency inhomogeneity, but requiring some interaction to provide tissue training pixels and to perform post processing adjustments [14, 15]. The parametric probabilistic classification is sensitive to accurate estimation of the probability density function [16]. Nonparametric approaches obtain the parameters of the probability density function from data without any assumptions, so these approaches are accurate, but expensive [17, 18]. Computational complexity and low generalization of trained classifiers limit their applicability. Unsupervised methods employed for MR brain image segmentation include k-means and its fuzzy equivalent Fuzzy c-means [19]. From a viewpoint of reproducibility, unsupervised methods are clearly desirable. Many algorithms are introduced to make Fuzzy c-means robust against noise and inhomogeneity, but most of them still present low accuracy [20, 21]. Other pattern recognition methods such as neural networks and template matching have been also applied to MR brain image segmentation [21, 22].

Edge-based segmentation approaches have been widely investigated to segment MR images of the head [1, 23, 24]. Base methods apply local operations to every point of the input picture, in order to extract short edge elements. Some of these operations are very simple, such as the gradient or the Laplacian, whereas other operations are more complex and allow the elimination of most of the local noise [25]. When small edge elements have been obtained, edge following strategies are applied to connect them to form borders. Snell *et al*. used an active surface template to find the intracranial boundary in MRI volumes of the head [26]. The method is based on the active contour model algorithm 'Snakes' [27]. However, the resulting procedure requires user interaction to provide a good initial contour for subsequent snake contour refinement. The Bayesian dynamic contour model [28] shows advantages over the snakes' active contour as the energy functions used to find the boundary can be more generally based on information about the whole region, rather than just the local boundary characteristics. The results are promising for the central slices of multispectral images presented, but have yet to be developed for isolating the whole brain. Contour-based deformable models are applied successfully to MRI brain segmentation although the approach suffer from the difficulty of determining the initial contour and tuning parameters [4, 10]. Khotanlou *et al*. [4] explicitly proposed a segmentation method based on deformable models and asymmetry analysis. Proceeding from the assumption that in normal brain the symmetry plane of the head is approximately equal to the symmetry plane of the segmented brain, an MRI brain segmentation algorithm robust in presence of tumor has been developed. Results obtained are satisfactory, but they heavily depend on the validity of the symmetry assumption. A boundary tracing method using dynamic programming for noisy brain sections with vague boundaries is proposed, but successful application for global segmentation of MR images remains to be demonstrated because a good initial guess for the boundaries is required [29]. Of the many techniques available for automated

DOI: 10.1002/cnm

border detection, those based on graph searching principles [30] have been successful in several applications. The value of graph search method lies in robustness, which derives from the property typical of the optimization methods of embedding global information about edges and the structure of object in a figure of merit allowing accurate border detection from noisy pictures [31]. Graph searching has become one of the best investigated segmentation tool for medical image data with applications to coronary angiography, ultrasound and cardiac MRI imaging [32–35]. However, to the best of our knowledge, the application of this technique to MRI brain segmentation has not yet been investigated.

In the present work, we focus our attention on fully automatic whole brain segmentation from MRI volumes, specifically addressing those critical situations in which the presence of pathologies such as tumors of great dimension and/or with location close to the border causes significant morphological deformations and consistent alteration of homogeneity. We derive our method from the edge-based approach adopting graph searching technique [30] for 2D boundary detection. The solutions investigated in this paper are an extension of those adopted in a previous work [31] from which we inherit the graph searching model. The MRI volume is processed slice by slice; the overall segmentation procedure is made fully automatic and easily reproducible by the automatic detection of frames including eyes and by computing the internal main parameters directly from the image data.

Several experiments were conceived and conducted to evaluate qualitatively and quantitatively the segmentation method proposed using a varied set of pre-surgical and post-surgical MR data from patients with cerebral tumors. A first set of experiments addressed the question of how did the performances of the proposed method depend on its main parameters. A second set of experiments was aimed to assess the accuracy of the solutions proposed for the automatic detection of the frames including eyes. A third set of experiments was aimed to evaluate robustness of the method in segmenting images with increasing levels of pathological deformation. Finally, to investigate whether the proposed segmentation can be considered an alternative to current well known solutions, a detailed comparison analysis was conducted using segmentation procedures available in FSL software tool [6].

2. GRAPH SEARCHING TECHNIQUE FOR RADIAL CONTOUR DETECTION

The salient aspect of our approach to whole brain segmentation is the use of graph searching for identifying optimal brain borders. Brain contour has a radial shape that can be conveniently treated by using polar coordinates. We proceed then by formulating graph searching conceptual ingredients for contour detection in polar space [30, 36]. Let $I_{\mathrm{cart}}(x, y)$ be an image described on a square cartesian discrete grid. The image can be 'unwrapped' converting it in polar coordinates, obtaining $I_{\mathrm{pol}}(\rho, \theta)$ where $1 \leqslant \rho \leqslant M$, $1 \leqslant \theta \leqslant N$, $\rho = \sqrt{(x-x_o)^2 + (y-y_o)^2}$, $\theta = \arctan\left(\frac{y-y_o}{x-x_o}\right)$ and (x_o, y_o) coordinates of the centroid of the object. Working in polar space, the radial boundary of a given object can be represented by a transformation $\rho = f(\theta)$ characterized by the following feasibility constraints:

Boundary as a function - $f(\theta)$ is single valued, and the value ρ exists for each θ with $1 \leqslant \theta \leqslant N$
Connectivity constraint - $|f(\theta+1) - f(\theta)| \leqslant 1$ for $1 \leqslant \theta \leqslant N-1$
Closing constraint - $|f(1) - f(N)| \leqslant 1$ imposing that the first and last pixels satisfy the connectivity constraint.

Each feasible function $f(\theta)$ is a candidate object boundary. The goal is then to find the minimum cost boundary subject to the feasibility constraints. The boundary detection task within the graph searching framework is modeled by embedding the properties of the boundary in a cost function, and formulating the boundary extraction as the problem of minimizing this function subject to the feasibility constraints. The boundary cost is defined as follows:

$$B_{\mathrm{cost}} = \sum_{\theta=1}^{N} C(\theta, f(\theta)) \tag{1}$$

DOI: 10.1002/cnm

where $C(\theta, f(\theta))$ is a cost image. The value of each pixel in the cost image must be inversely related to the likelihood that an edge is present at that point. The likelihood is usually determined by the application of a low-level local edge operator [32]. In general, the definition of this cost function depends on a priori knowledge on the object to be segmented. The boundary cost allows to express both local and global information that can be incorporated within the constrained minimization strategy for optimal boundary detection. Representing the constrained minimization problem within the graph search framework, a graph is built where nodes are cost image pixels whose values are node weights. The connectivity of the graph is derived from the feasibility constraints. Minimal cost feasibility boundary is the minimum cost path in the weighted node graph that can be identified by using A* Algorithm [36].

The global solution is implemented by a bottom-up scheme: the solution of the whole problem is built from the solutions of the subproblems. A 'path cost image' collecting the intermediate information useful for defining the global optimal solution is computed with the Algorithm 1. In the path cost image, the minimum value of the last column is the cost of the minimal path. Starting from this point and passing through the graph up to the first column, the minimal path is found by choosing for each visited point the adjacent nodes having the minimum value. In this way, the feasible function that minimizes the cost is detected. Figure 1 shows the steps with which the 2D segmentation method based on graph searching is organized. Figure 1(b) shows the polar representation of the original radial object represented in cartesian space (Figure 1(a)). In Figure 1(c), the superimposition of the minimum path on the cost image is shown. Figure 1(d) represents the solution in the original cartesian space.

Algorithm 1 algorithm for computing the Path Cost Image P basing on the cost image C

for $j = 0$ to M-1 **do**
  $P(j, 1) \leftarrow C(j, 1)$
end for
for $i = 1$ to N-1 **do**
  for $j = 0$ to M-1 **do**
    if $i = 0$ **then**
      $P(j, i) \leftarrow C(j, i) + min(P(j, i-1), P(j+1, i-1))$
    else
      if $i = N - 1$ **then**
        $P(j, i) \leftarrow C(j, i) + min(P(j, i-1), P(j-1, i-1))$
      else
        $P(j, i) \leftarrow C(j, i) + min(P(j-1, i-1), P(j, i-1), P(j+1, i-1))$
      end if
    end if
  end for
end for

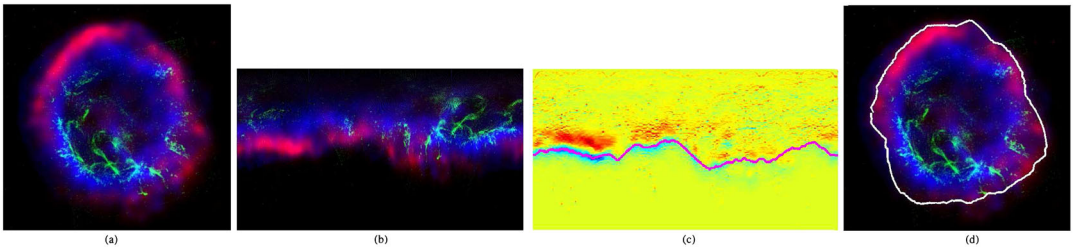

Figure 1. Sequence of the steps where the 2D segmentation method based on graph searching is organized: (a) Cartesian image; (b) polar image; (c) superimposition of the minimum path on the cost image; and (d) segmentation result.

DOI: 10.1002/cnm

3. GRAPH SEARCH TECHNIQUE FOR BORDER DETECTION IN BRAIN MRI

In this section, the application of the previously described general framework to the solution of whole brain segmentation in MRI imagery is detailed, addressing specific imaging related aspects. We consider that between the brain and the skull, there is a layer of liquor, and in the MRI imagery used in our study, this anatomical part is acquired with voxel values close to zero. Secondly, we take into account that the bone is more intense than the brain tissue, and the transitions from the brain and the 'liquor cushion' and from the skull and the external air are similar and can be confused as shown in Figure 2. Proceeding from these considerations, a first cost image with which to identify the internal skull boundary is firstly defined; the actual cost image for the brain boundary detection is subsequently defined after a masking procedure. The overall detection procedure includes a preprocessing phase aimed to emphasize the brain boundary before starting with the boundary graph-based detection. The more the object is similar to a circle in Cartesian coordinates or, in other words, a horizontal line in the θ, ρ plan, the more the description of the cost through the Sobel filter application is effective. In axial images of the brain, this feature is very strong and could be easily emphasized by changing the aspect ratio of the image. After this preprocessing phase, the 2D brain segmentation is accomplished in the three following phases.

Phase 1. Polar conversion - The image is converted in polar coordinates. The polar sampling is a topic widely discussed in literature, presenting a high level of complexity if optimally solved [37]. In this work, we adopt a sub-optimal solution considering a square grid for the description of the polar space and using an average filter applied on the polar image.

In order to fulfill the fully automation requirement, both the angular sampling and the center of the polar space are automatically computed from the data. Let $A_{\max}$ be the major axis of the ellipse that circumscribes the image points whose intensity is higher than average $[x_+, y_+]$, the number of angle N_{ang} is computed as follows:

$$N_{\text{ang}} = \pi A_{\max} \tag{2}$$

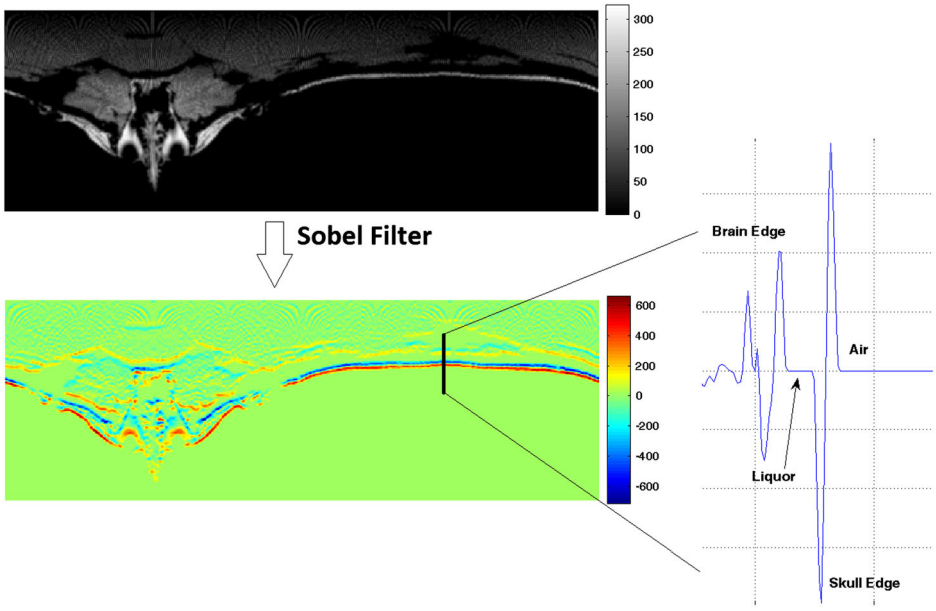

Figure 2. Polar representation of brain axial slice and result of the vertical Sobel filter application, with emphasis on a vertical line of profile.

DOI: 10.1002/cnm

and the coordinates of the center of the polar space (x_o, y_o) are computed as the centroid coordinates of the points $[x_+, y_+]$; formally

$$x_o = \frac{1}{N_{x_+}} \sum_{i=1}^{N_{x_+}} x_{+,i}; \quad y_o = \frac{1}{N_{y_+}} \sum_{i=1}^{N_{y_+}} y_{+,i}.$$

The resulting centroid coordinates approximate the actual brain centroid with an estimation error related to the accuracy of the segmentation by trivial thresholding. We have experimentally verified that the approximation does not affect the graph segmentation results (Section 4).

Phase 2. Skull boundary detection - The cost image is computed by applying the vertical Sobel filter to the polar image. Every pixel of this cost image is a weight of graph nodes, and using the feasibility constraints, the graph connections are identified. The minimal path in the graph is computed using Algorithm A*, and skull boundary is found. A binary mask is computed distinguishing between pixels with ρ less and greater than the edge. This mask is applied to cost image, and it is inverted to find a new cost image for the second step: the actual brain segmentation.

Phase 3. Brain boundary detection - The Algorithm A* for the extraction of the minimal path is applied on this new cost image. The minimal path in the graph is the brain boundary in the polar space. The last step is the conversion, in Cartesian coordinates, of the detected boundary.

The schema of the overall 2D brain segmentation procedure is shown in Figure 3.

The detection of the 3D boundary of the brain is computed iterating the 2D segmentation process on every slice composing the whole brain. Often, the brain MRI volume starts from the shoulders and includes a portion of air above the head, especially if we consider axial slices of a volume acquired trough subsequent sagittal sections. It would not be appropriate to compute the initial and the final image slice to be processed in the volume as a percentage of the number of slices because

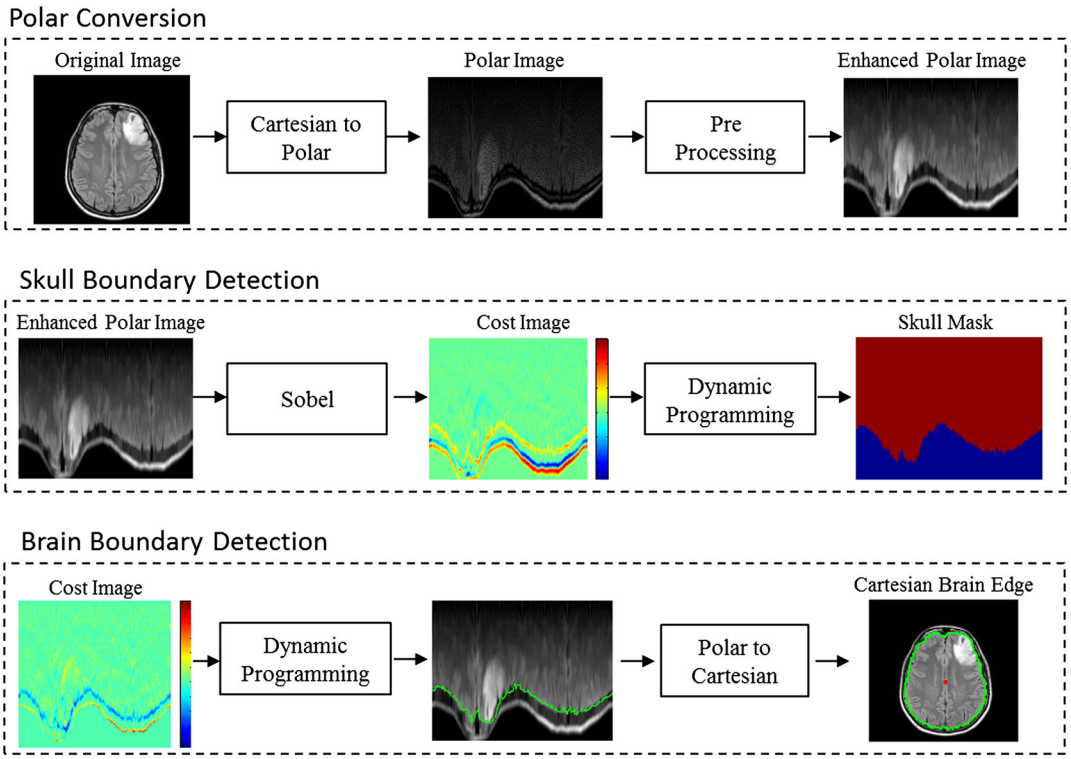

Figure 3. Two-dimensional brain segmentation strategy.

DOI: 10.1002/cnm

parts of the body included in the volume vary greatly depending on the acquisition mode and on the inter-subject variability. To make our technique completely independent from the acquisition mode and fully automatic, both the starting and stopping slices are computed directly from the data. The final slice is identified by segmenting the central sagittal slice with the algorithm detailed earlier. Let $\boldsymbol{r}$ and $\boldsymbol{c}$ be two vectors containing the row and column values of the pixels belonging to the segmented portion, respectively; the final slice is $\mathrm{Stop} = \min(r)$.

Instead, the initial slice is related to the first slice containing the eyes S_e. The eyes detection is a widely studied topic especially in biometric application [38, 39]. Considering that the main feature of the eyes is the circular shape, the slice of interest (SoI) detection is performed in the Hough Transform domain [40]. This approach is a well-known feature extraction tool, applied on a thresholded edge image. The Hough Transform allows to obtain an accumulation matrix in which the intensity peaks correspond to the position of the center of the circular objects with a specific radius in the image. The eyes radius, very stable in our data, is set to 1-cm value. The SoI detection procedure is detailed as follows. The edge extraction process is composed of three phases iterated for each slice:

- The image is thresholded looking at values greater than zero.
- A close morphological operation is applied on the binary image, with a circular structural element with radius less than 1 cm.
- Edges are extracted using Sobel filter applied on the image.

The Hough transform is applied on the binary edge image, and the accumulation matrix A is computed. In Figure 4, three examples of the previously detailed process are shown. Figure 4(a) and (b) shows the processing of a slice under the SoI, at the dental arch level and a slice over the SoI, respectively. The third case (Figure 4(c)) is related to the SoI.

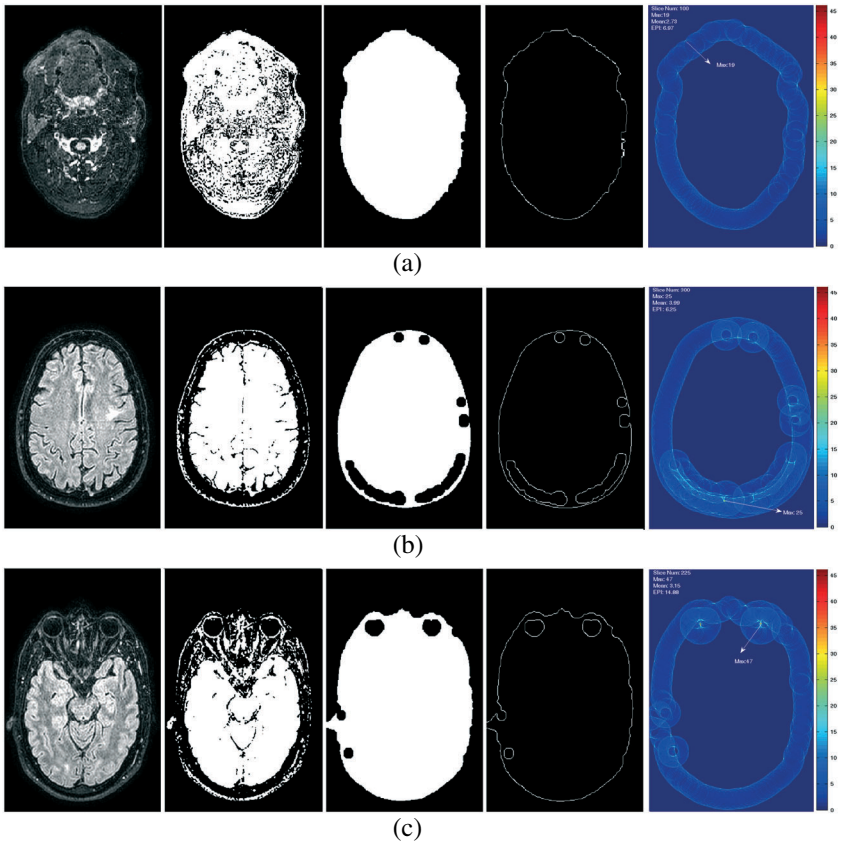

Figure 4. Phases of the eyes slice detection algorithm: (a) slice at the dental arc level under the slice of interest (SoI); (b) slice over the SoI; and (c) SoI.

DOI: 10.1002/cnm

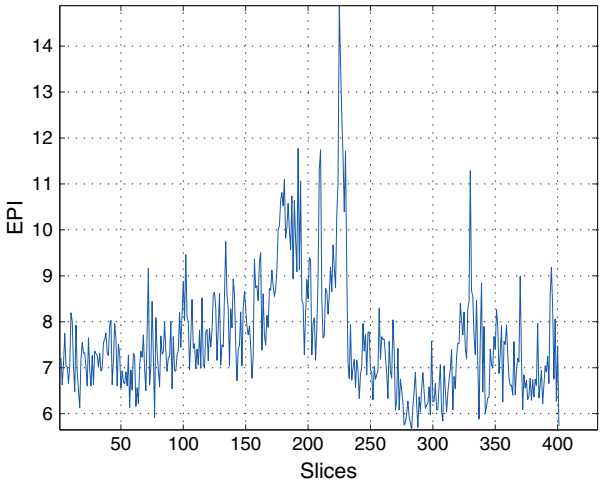

Figure 5. Eyes presence index signal.

For each slice in the volume, an eyes presence index (EPI) is computed. Let A^i be the accumulation matrix related to the ith slice with dimension $[J \times K]$ the EPI is obtained as follows:

$$\tilde{A}^i = \left\{ \tilde{a^i} \mid \tilde{a^i} = a^i_{j,k} \quad \wedge \quad a^i_{j,k} > 0 \quad \text{for} \quad 1 \leqslant j \leqslant J \quad \text{and} \quad 1 \leqslant k \leqslant K \right\};$$

$$EPI(i) = \frac{\max(\tilde{a^i})}{\frac{1}{W}\sum_{w=1}^{W} \tilde{a^i_w}}$$

where W is the cardinality of $\tilde{A}^i$, then the SoI is computed as follows:

$$SoI = \underset{i}{\operatorname{argmax}}\, EPI(i) \tag{3}$$

The EPI(i) values in the three examples given earlier are respectively: 6.25, 6.97, 14.88, the eyes slice has an EPI(i) value greater than twice the other two. In Figure 5, an example highlighting the significance of the EPI index is shown in function of the slice number. In Section 4.2, a statistical significance of EPI is analyzed. The SoI identifies the central slice of the eyes. The starting slice is computed by shifting the SoI of a number of slices equal to the radius of the eyes.

4. EXPERIMENTAL RESULTS

Many experiments were conceived and conducted to assess the performances of the algorithm, both qualitatively and quantitatively. The dataset used for the evaluation process is composed of 14 FLAIR MRI gray scale, 12-bit-depth volumes. All dataset volumes are altered by the presence of glial tumors heterogeneous in terms of position, dimension, intensity and shape. As detailed in Table I the dataset is composed of two parts. The first 10 MRI images are obtained with a FLAIR sequence; the slice thickness is 5 mm, the sequence is characterized by long repetition times and by a reversal of the spin pulse at 180°; the measurement is performed when the value of the liquid is close to 0 allowing the removal of the signal of liquid normally hyper-intense in sequences with long repetition time. The cases 9 and 10 are post surgical MRI playing the role of assessing the performances of our segmentation strategy also in cases where the most commonplace assumptions about the shape of the brain such as symmetry are lacking.

The second part of the dataset is composed of volumetric acquisition with isotropic voxel (0.57 mm). This high resolution allows to detect fine anatomical detail, to reconstruct on different orthogonal planes (axial, sagittal, coronal) and to make accurate measurements. These advantages, however, are obtained at the expense of signal to noise ratio. The results obtained from the varied

DOI: 10.1002/cnm

Table I. Data set description.

Case	Acquisition mode	Volume size (voxel)	Slice thickness	Spacing between slice	Pixel spacing	Repetition time	Echo time
1	Assial FLAIR-T2	[228 × 228 × 22]	5	6	(0.80,0.80)	11000	140
2	Assial FLAIR-T2	[320 × 320 × 23]	5	6	(0.75,0.75)	11000	140
3	Assial FLAIR-T2	[228 × 228 × 23]	5	6	(0.80,0.80)	11000	140
4	Assial FLAIR-T2	[320 × 320 × 23]	5	6	(0.75,0.75)	11000	95
5	Assial FLAIR-T2	[256 × 204 × 20]	5	6	(0.94,0.94)	7800	95
6	Assial FLAIR-T2	[256 × 204 × 20]	5	6	(0.90,0.90)	7800	95
7	Assial FLAIR-T2	[256 × 204 × 20]	5	6	(0.90,0.90)	7800	95
8	Assial FLAIR-T2	[256 × 204 × 20]	5	6	(1.02,1.02)	7800	95
9	Assial FLAIR-T2	[256 × 204 × 20]	5	6	(0.98,0.98)	7800	95
10	Assial FLAIR-T2	[256 × 204 × 20]	5	6	(0.98,0.98)	7800	95
11	Sagittal FLAIR-T2	[432 × 432 × 300]	0.6	0.6	(0.57,0.57)	8000	282.89
12	Sagittal FLAIR-T2	[432 × 432 × 300]	0.6	0.6	(0.57,0.57)	8000	281.93
13	Sagittal FLAIR-T2	[432 × 432 × 300]	0.6	0.6	(0.57,0.57)	8000	281.38
14	Sagittal FLAIR-T2	[432 × 432 × 300]	0.6	0.6	(0.57,0.57)	8000	282.43

set of experiments have been evaluated qualitatively by a group of experts by comparing the results produced by the automatic segmentation with those obtained by manual segmentation.

In order to limit the effects of the well-known phenomenon of inter-observer and intra-observer variation, our strategy contemplates the organization of 'tuning sessions' aimed at establishing a consensus among experts through discussion of the most controversial segmentation cases.

An analysis of the stability of the results in function of the variations of the center coordinates in the polar reference system was performed. The eyes slice detection algorithm is tested on all the dataset volumes, and the statistical significance of the EPI index is proved.

The last section of the experimental phase is about the comparative analysis between our algorithm and a well known and more used segmentation algorithm: FEAT FSL Brain Extraction Tool (BET) [6] that uses a deformable model, which evolves to fit the brains' surface. Segmentation results shown in Figure 6 are obtained by processing five slices at different levels from the same MRI volume (Figure 6(a)), and five slices from different cases (Figure 6(b)). In the first row of both Figure 6(a) and (b), the original slices are displayed; in the second, the boundary detected by the algorithm is superimposed on the original image, and in the last row, the brain extraction is shown.

The team of experts performed a visual inspection of the resulting segmented images judging satisfactorily the results obtained also in cases in which tumors are very invasive. The segmentation procedure has a good behavior also when processing critical slices such as those including eyes or slices near the top skull, characterized by high texture and complex morphological patterns.

In Figure 7(a) and (b), two examples of post surgery MRI are shown. One of the goals of the post-operative MRI inspection is to identify any tumor residual. In this context, the whole brain segmentation is used as a preprocessing phase for subsequent tumor detection, segmentation and analysis. The whole brain segmentation strategy has to be able to reach accurate and robust results even when the most commonplace assumptions about the brain are lacking. The removal of the expansive mass cause morphological and signal alterations.

In the first case (Figure 7(a)), an uneven area can be seen at the site of intervention because of the surgical cavity in which cerebrospinal fluid is observed, together with traces of blood and air bubbles. It is visible that a rim of perilesional edema (hyperintense) and into the deepest parts, in the vicinity of the lateral ventricle, the signal hyperintensity is consistent with a small tumor residual. Among the brain and the opercolo, which has been repositioned at the end of the intervention, there is a small flap hyperintense, consistent with a subdural flap, located in the meningeal subdural space between the brain and the skull, with a maximum thickness of 5 mm. Outside of the skull, there is an important thickening of the subcutaneous tissues overlying the operculum, clearly uneven, caused by edematous imbibition. In the outer part, there are the stitches with a typical signal distortion. Again in Figure 7(b), an MRI after surgical removal of right frontal expansive mass is shown.

DOI: 10.1002/cnm

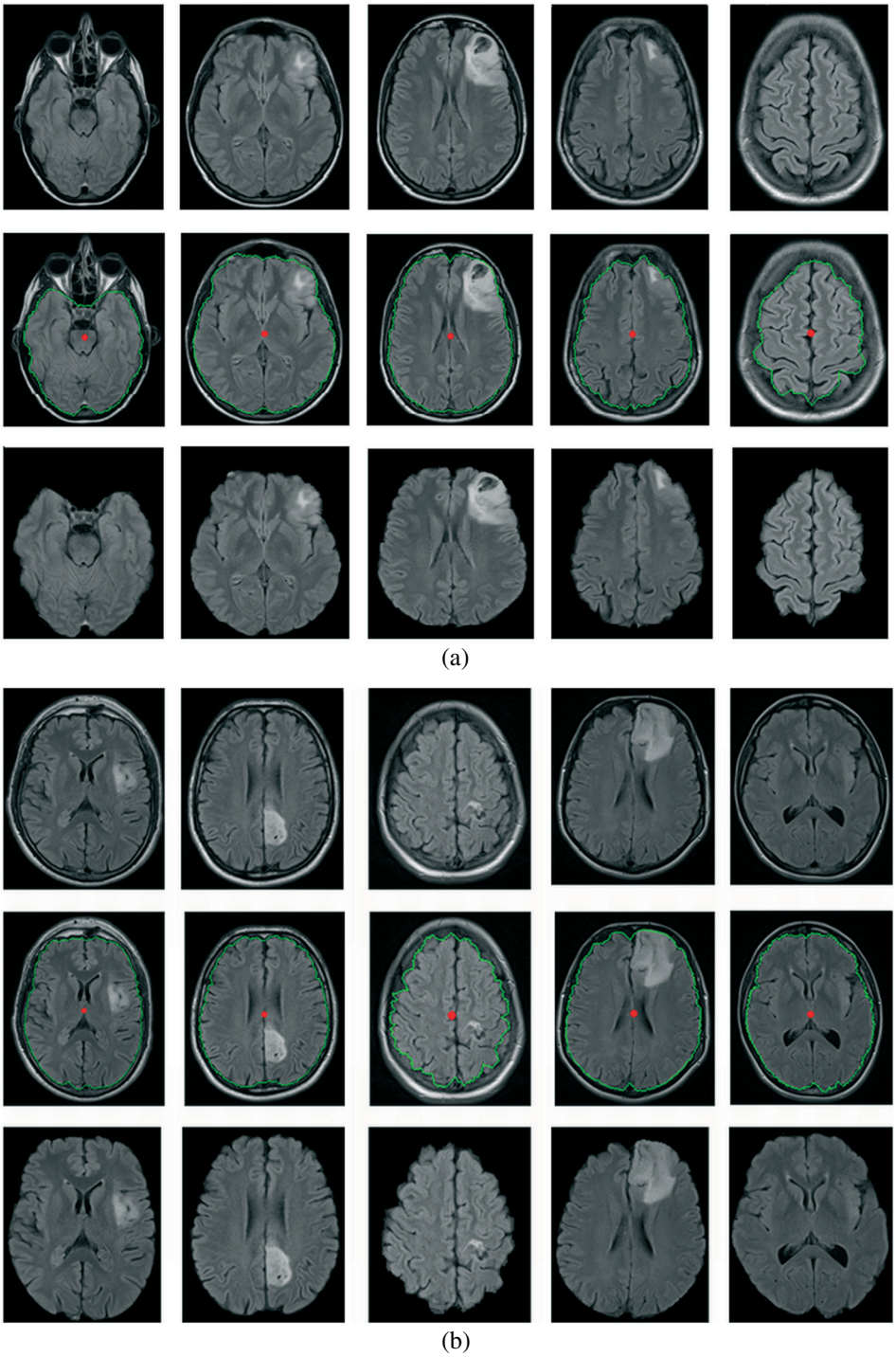

Figure 6. Example of 2D brain segmentation: (a) different slices of the same patient and (b) different patients.

Contrary to the previous case, here, the operculum was removed to allow decompression of the brain around the lesion, hyperintense edema-gliotico halo is visible: small right frontal subdural flaps with a maximum thickness of 3 mm. All these anomalies compared with the structure of a standards brain MRI, make the automatic brain segmentation a hard task. Moreover, the high variability between the cases highlights the need for a robust algorithm working without a priori conditions to solve the

DOI: 10.1002/cnm

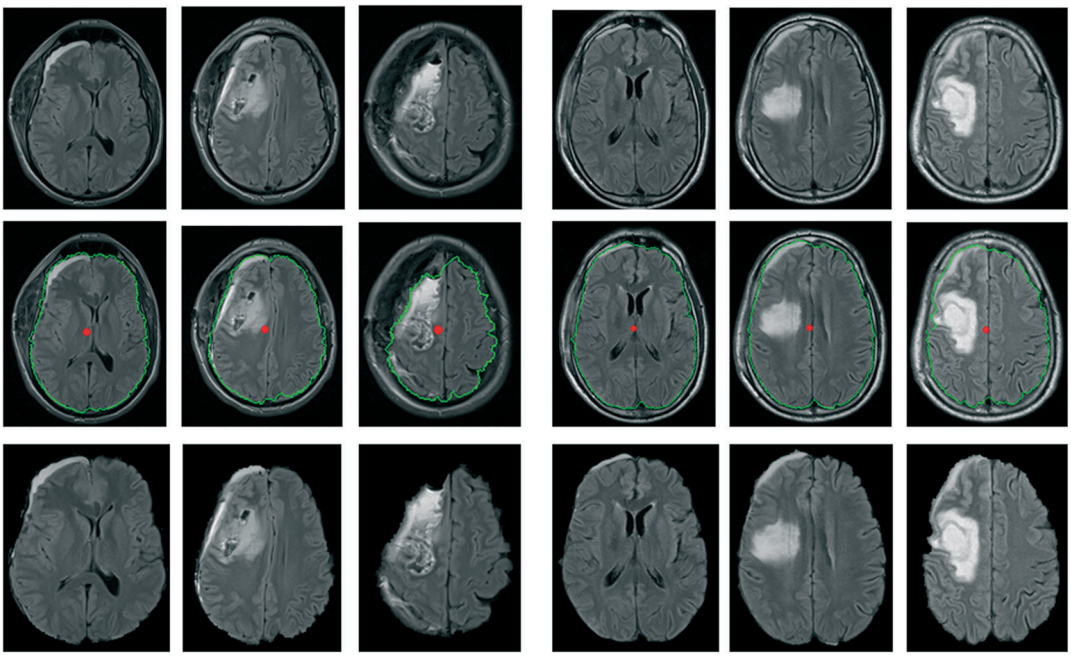

Figure 7. Post surgery examples.

segmentation problem. In both cases, the segmentation algorithm results have been well evaluated by the experts. The presence or absence of the operculum, the asymmetries and large deformations, do not affect the performance.

The quantitative analysis is conducted on the volumetric MRI (cases 11–14). For each volume, the segmentation results, related to 10 slices evenly sampled, are evaluated in terms of both surface estimation and segmentation similarity. For each selected slice, a ground truth mask has been manually identified and used in the evaluation. As regards the evaluation of the algorithm capability to estimate the surface, the error made is computed by $E = (S_{\text{true}} - S_{\text{alg}})/S_{\text{true}}$ where S_{true} is the mean of the surface obtained by the manual labeled masks produced by individual experts, and S_{alg} is the surface of the region detected by the segmentation algorithm. As regards the segmentation similarity, three performance indexes are used: the Jaccard index $J = \frac{T_p}{T_p+F_p+F_n}$ [41], the Precision $P = \frac{T_p}{T_p+F_p}$ and the Recall $R = \frac{T_p}{T_p+F_n}$ [42] where Tp are true positive, Tf true negative, Fp false positive and Fn the false negative. Table II reports results for both surface and similarity evaluations. Performances are highly satisfactory with mean value of Jaccard, Precision and Recall indexes equal to $\bar{J} = 91,43$, $\bar{P} = 93.36$, $\bar{R} = 97.78$, respectively. It is worth to note that there is a common trend through the slices in all four cases. Indeed, best results are obtained in central slices (35–110) with mean values $\bar{J} = 96.55$, $\bar{P} = 98.314$, $\bar{R} = 98.35$; results slightly decrease overestimating at eye level (Slices 5,20) with mean values $\bar{J} = 86.15$, $\bar{P} = 87.72$, $\bar{R} = 98.89$. The worst performances are found in the top slices with mean values $\bar{J} = 80.98$, $\bar{P} = 84.15$, $\bar{R} = 95.53$. In the last column of Table II, the expert variability, measured with Jaccard index, is reported making transparent the level of inconsistency under which the quantitative evaluation process has taken place.

4.1. Sensitivity analysis

As previously mentioned, the identification of the center of the polar reference system is a critical aspect in the overall procedure. A sensitivity analysis is conducted with the aim of measuring how the segmentation accuracy depended on this parameter. Varying the center of polar image, different optimal feasible functions are obtained. Differently from the number of polar angle parameters

DOI: 10.1002/cnm

Table II. Quantitative analysis.

Case	Slice	S_{gt}	S_{alg}	E (%)	Jaccard (%)	Precision (%)	Recall (%)	InterJ (%)
1	5	11428.20	12111	5.97	82.57	88.44	99.02	97.58
1	20	13721.18	13732	0.08	96.67	98.27	98.35	97.12
1	35	14845.66	14920	0.50	97.00	98.23	98.73	97.23
1	50	15917.66	15942	0.15	97.81	98.82	98.97	97.88
1	65	15452.57	15548	0.62	97.42	98.39	99.00	97.32
1	80	14809.10	14746	0.43	96.44	98.40	97.98	97.40
1	95	13076.74	12910	1.28	96.88	99.05	97.79	96.88
1	110	10979.51	10216	6.96	91.74	99.25	92.39	94.58
1	125	7674.46	11632	51.56	60.80	62.76	95.12	91.39
1	140	3797.59	6995	74.20	54.51	54.52	99.95	93.12
2	5	10884.96	12897	18.48	81.98	83.07	98.43	95.44
2	20	13653.11	13697	0.32	97.94	98.80	99.12	97.86
2	35	15359.81	15357	0.02	95.67	97.80	97.78	97.77
2	50	15342.59	15431	0.58	97.76	98.59	99.15	97.72
2	65	15041.08	15150	0.72	97.36	98.31	99.02	97.86
2	80	14107.81	14272	1.16	97.40	98.12	99.26	97.93
2	95	12695.79	12769	0.57	96.12	97.74	98.30	97.23
2	110	10580.53	10412	1.59	95.69	98.59	97.02	97.51
2	125	7682.91	7760	1.00	94.36	96.61	97.58	96.09
2	140	4808.36	5179	7.71	68.66	78.48	84.59	91.83
3	5	6713.41	9860	46.87	58.29	58.34	99.79	86.37
3	20	10634.79	11168	5.02	91.50	93.28	97.96	96.45
3	35	13445.50	13221	1.67	95.35	98.45	96.81	96.76
3	50	15323.42	15512	1.23	97.85	98.31	99.52	97.84
3	65	15371.99	15517	0.94	97.73	98.39	99.32	97.83
3	80	14901.21	14990	0.60	97.92	98.66	99.25	97.83
3	95	13802.73	13949	1.06	97.54	98.24	99.28	98.00
3	110	12233.95	12453	1.79	96.54	97.37	99.12	97.52
3	125	10173.11	10079	0.92	96.47	98.65	97.76	95.84
3	140	7307.00	7429	1.67	94.20	96.22	97.82	95.22
4	5	10800,49	11847	9.68	89.23	90.15	98.88	96.88
4	20	13682,35	14897	8.88	91.03	91.42	99.54	97.06
4	35	15006,81	15213	1.38	96.95	97.78	99.13	97.60
4	50	15705,18	15921	1.37	97.54	98.08	99.43	97.76
4	65	15680,32	15848	1.07	97.54	98.23	99.29	99.76
4	80	15141,48	15288	0.97	97.69	98.36	99.31	97.87
4	95	14003,68	14014	0.07	96.14	98.00	98.07	96.57
4	110	12281,54	11968	2.56	93.99	98.17	95.67	96.09
4	125	9230,08	9211	0.21	95.40	97.75	97.54	95.50
4	140	6046,55	6431	6.35	83.41	88.24	93.86	93.08

whose setting simply affects the sampling rate, the variation of the center of polar reference system involves significant variation of the directional components of the polar image, and then vertical gradient values that are in correspondence with the likelihood that an edge is present at that point. We base our analysis on cases 1–8. For each volume, three slices are selected: one from the eyes level, the other two from central and top slices. For each selected slice with an independent procedure, we identify an ideal center. Under this condition, we proceed in the brain segmentation identifying the boundary $B_{\mathrm{cent}}(\theta)$ whose accuracy is qualitatively verified. We generate a set of new center coordinates moving randomly the centroid of N_p pixels. For each new generated center, the boundary $B_{\mathrm{move},Np}(\theta)$ is identified, and detection is evaluated as follows:

$$E_{N_p} = \frac{1}{N}\sum_{\theta=1}^{N}\frac{|B_{\mathrm{cent}}(\theta) - B_{\mathrm{move},Np}(\theta)|}{B_{\mathrm{cent}}(\theta)} \tag{4}$$

DOI: 10.1002/cnm

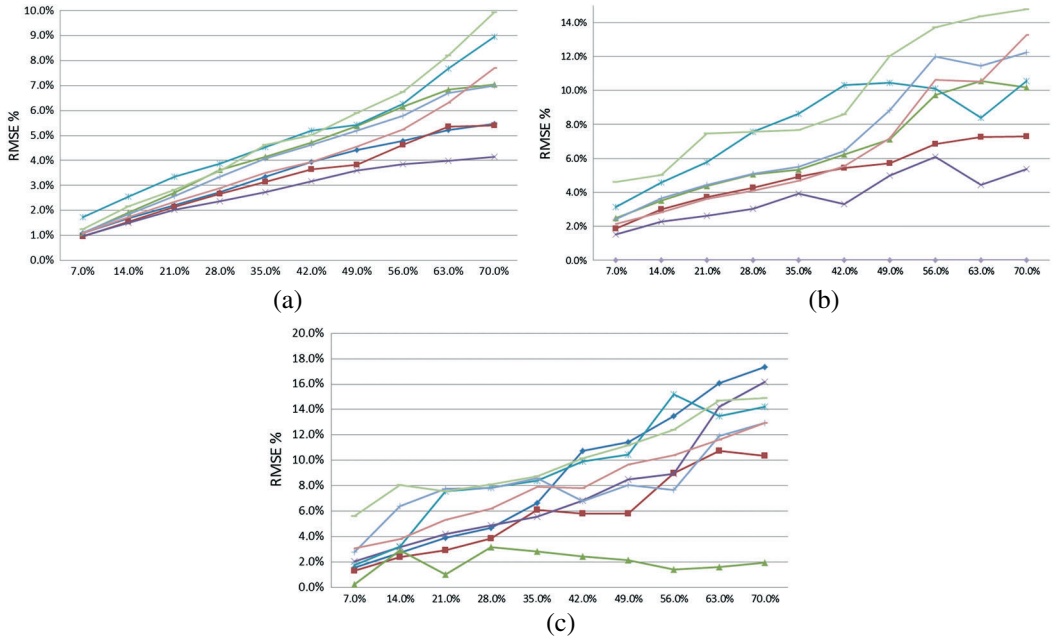

Figure 8. Stability analysis: Trend of errors as a function of the center deviation (a) central slice, (b) top slice, and (c) eyes slice.

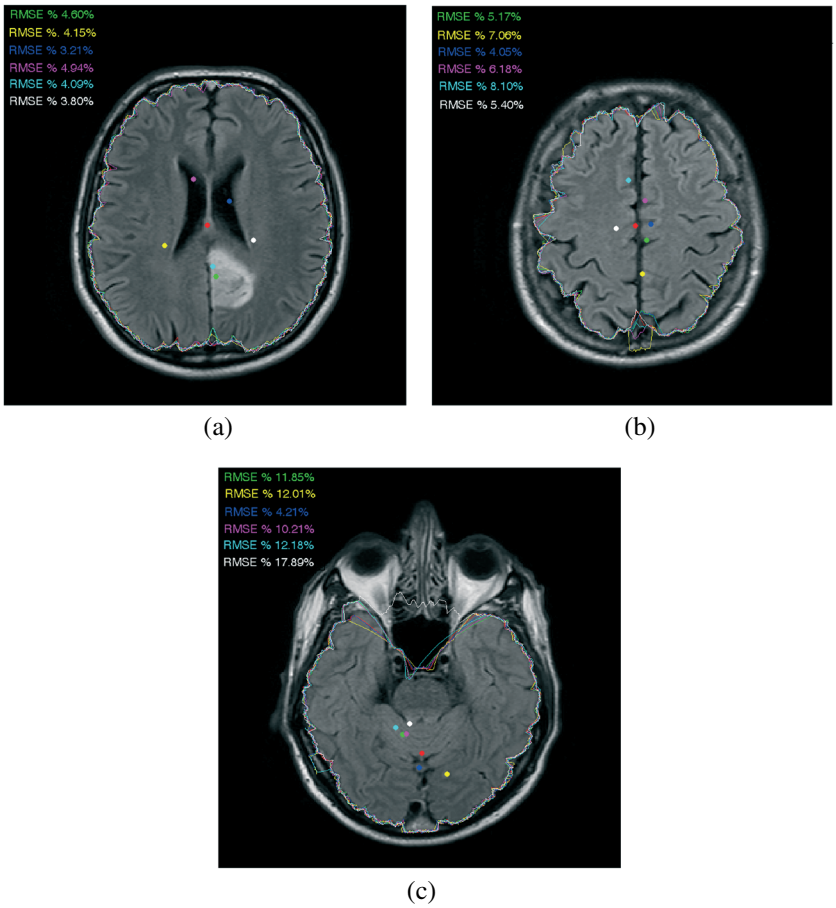

Figure 9. Stability analysis: Qualitative examples (a) central slice, (b) top slice, and (c) eyes slice.

DOI: 10.1002/cnm

where N is the number of sampled angles. For each N_p, the experiment is iterated for 50 trials, and the results are averaged. The results obtained form central top and eyes level slices are shown in Figure 8(a)–(c), respectively. The values N_p are expressed as a percentage compared with the maximin radius of the ellipse where the brain is inscribed, to make the results invariant to image resolution. The relation between errors and distances between the center of the polar system approximates a liner low. The interpretation of these results is twofold: the behavior of the system is predictable and controllable, and the variations of the parameter under study are not invasive. Moreover, the mean ratio between the percentage error and the percentage centroid deviation is equal to 0.11 for central slices, 0.17 for top slices and 0.21 for the eyes slices that show the higher instability.

To conduct a qualitative analysis in Figure 9, three visual examples are shown. The centers and the corresponding boundaries detected are superimposed on the MRI original slices. The visual and the earlier quantitative results analyzed tallied in general.

4.2. Eyes slice detection performance

The eyes detection procedure identifying the initial slice SoI of the volume segmentation is evaluated by comparison with a manual detection using all the 14 cases of the dataset. The manual procedure is based on the identification in each volume of the first and last axial slices containing eyes; the slice lying in the middle between these two is considered as ground truth SoI_{gt} in the evaluation procedure. For each volume, we compute the detection error $E = |SoI_{\mathrm{gt}} - SoI|$, which is expressed in terms of number of slices; using the *slice thickness*, which is accessible in the DICOM header, it is converted into millimeters. Table III details the obtained results. The first 12 cases show errors always smaller than 5 mm, under the vertical resolution of the voxel, except for case 1 in which the error is equal to the vertical voxel resolution.

Table III. Eyes detection results.

Case	Start eyes	Stop eyes	SoI	E	EPI	EPI mean
1	6	10	9	5	13.84	6.79
2	5	10	7	2.5	14.40	7.55
3	7	10	9	2.5	10.82	7.63
4	4	9	7	2.5	10.05	6.75
5	3	8	5	2.5	8.58	5.37
6	5	9	7	0	11.09	6.78
7	6	9	8	2.5	10.98	6.95
8	6	9	7	2.5	12.24	6.77
9	5	10	8	2.5	11.89	6.66
10	5	8	7	2.5	11.14	6.97
11	209	242	225	0.3	14.88	7.01
12	190	227	215	3.9	15.12	7.30
13	175	208	189	1.5	15.32	7.81
14	200	235	218	0.3	15.69	7.31

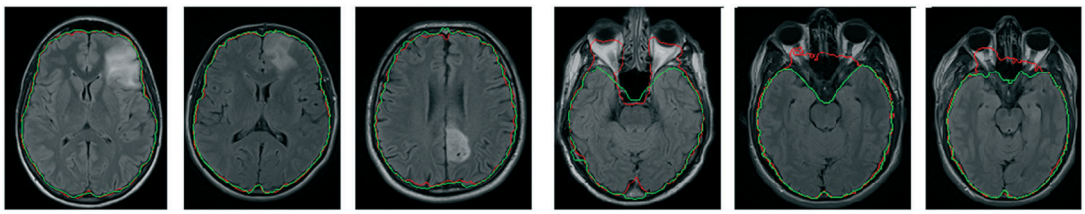

(a) (b)

Figure 10. Performance comparison of our algorithm versus FSL BET: (a) central slice, good overlap and (b) slices at the eyeball level, bad overlap.

DOI: 10.1002/cnm

For what concerns the volumetric images 11–14, in two cases (11,14), the error is less than the slice thickness (0.6 mm); for the cases 12 and 13, the error is 1.5 and 3.9 mm, respectively. These results can be reconducted to a slight variation of eyes diameter. In the last two columns of the table, there are the EPI values of the detected slices and the mean values of the EPI signal computed for every slice, respectively. Basing on the results obtained, we may conclude that the EPI index

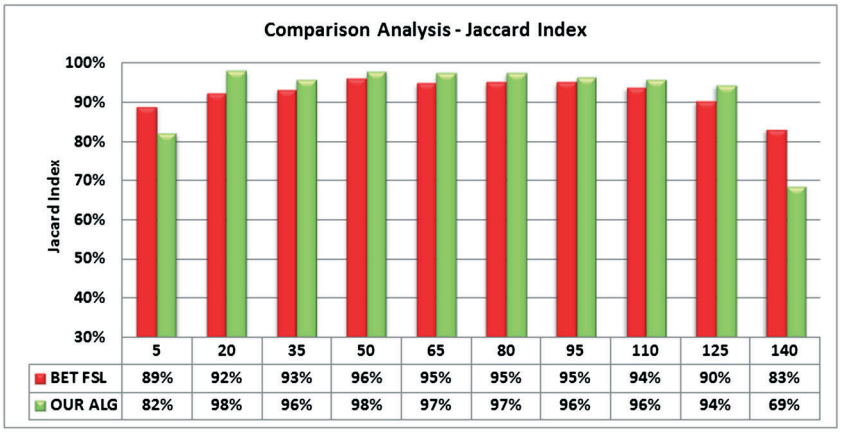

	5	20	35	50	65	80	95	110	125	140
BET FSL	89%	92%	93%	96%	95%	95%	95%	94%	90%	83%
OUR ALG	82%	98%	96%	98%	97%	97%	96%	96%	94%	69%

(a)

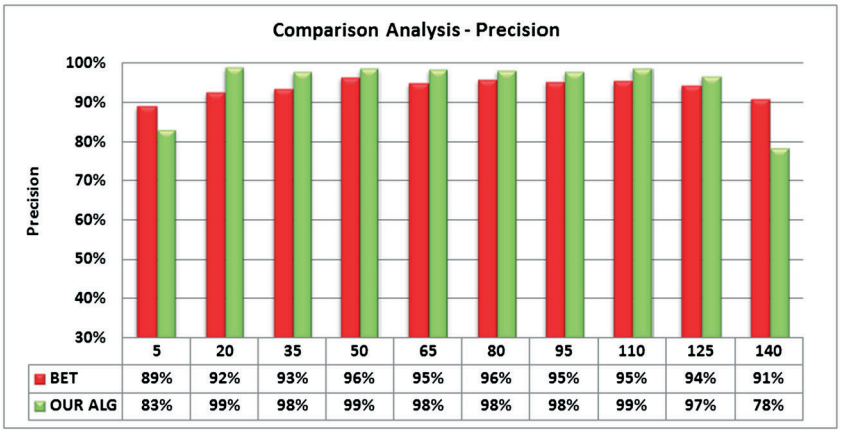

	5	20	35	50	65	80	95	110	125	140
BET	89%	92%	93%	96%	95%	96%	95%	95%	94%	91%
OUR ALG	83%	99%	98%	99%	98%	98%	98%	99%	97%	78%

(b)

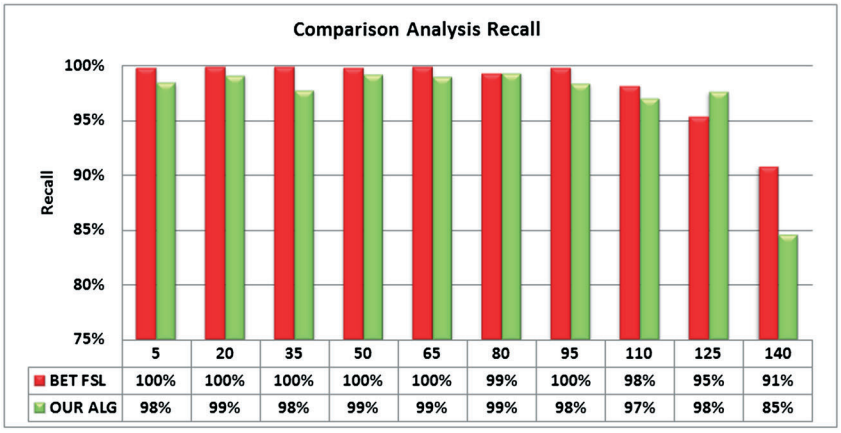

	5	20	35	50	65	80	95	110	125	140
BET FSL	100%	100%	100%	100%	100%	99%	100%	98%	95%	91%
OUR ALG	98%	99%	98%	99%	99%	99%	98%	97%	98%	85%

(c)

Figure 11. Quantitative Comparison of our algorithm versus FSL BET: (a) Jaccard, (b) Precision, and (c) Recall.

DOI: 10.1002/cnm

is robust considering the separability of the mean of EPI signal and the EPI value of the detected slice. The distribution separability was evaluated with a *t*-test obtaining a confidence value equal to 99.96%

4.3. Comparison analysis

Our strategy has been compared with the widely used FEAT FSL Brain Extraction Tool (BET) [6]. The BET algorithm describes the brain surface starting from a sphere composed of vertices, and triangles obtained by dividing iteratively the triangles of an icosahedron; each surface vertex is iteratively moved by a set of forces, which consider the homogeneity of the region inside the surface and the intensity of the transitions. A qualitative comparison has been conducted using cases 1–8; cases 11–14 have been compared quantitatively. In Figure 10, some examples of the comparison are shown. The brain boundaries are superimposed on six MRI slices. The red boundary is found by using the BET, and the green one with our method. When processing the central slices, the two techniques have comparable behavior (Figure 10(a)); when processing eyes level slices (Figure 10(b)) our strategy definitely prevails. The results can be interpreted in the light of the fact that the embedding of both the local and global information in the graph search segmentation allows to identify the complete brain boundary even in a complex scene. Instead, the BET deformable model strategy is deceived by high-transition zone related to different anatomical parts. The ground truth masks and the evaluation metrics described earlier are used to develop the quantitative analysis. The analysis is focused on cases 11–14 that record scenes in which the transition between the tissue are shaded and the noise level is high. Results obtained for all cases considered (11–14) highlight a comparable behavior with slightly better performance of the BET when processing eyes and top level slices. As mentioned earlier, the edges are shaded, thus the BET is not deceived by high-transition zone related to different anatomical structure. Moreover, it is worth to note that BET is a 3D algorithm that considers connectivity information in all directions. For these reasons, it shows advantages in cases in which the segmentation tasks are more difficult at the eyes and top level. Figure 11 shows the comparison analysis for an illustrative example related to case 11.

5. CONCLUSION

In this paper, we have presented a strategy to segment whole brain in MR images. The strategy exploits a 2D graph-based technique to reliably detect boundary in complex scenes characterized by heterogeneous morphological patterns. A full level of automation is achieved through the automatic detection of frames including eyes and the computation of values for internal main parameters directly from the image data. As seen in our experimental context, the overall segmentation procedure is less sensitive to parameters variations, it shows a robust behavior while segmenting images with increasing levels of pathological deformation and has proven competitive compared with standard state-of-the-art solutions. It is then eligible as an operational tool specifically oriented to actively support surgical planning and post-surgical assessment activities. The encouraging results we have obtained in this work prompted us to continue with further work that will aim to improve the quality of segmentation results. In particular, our purpose is to extend the present solutions taking into account the information available in the spatial sequence of MRI images forming the 3D data.

REFERENCES

1. Clarke LP, Velthuizen RP, Camacho MA, Heine JJ, Vaidyanathan M, Hall LO, Thatcher RW, Silbiger ML. MRI segmentation: methods and applications. *Magnetic Resonance Imaging* 1995; **13**(3):343–368. DOI: 10.1016/0730-725X(94)00124-L.
2. Balafar M, Ramli A, Saripan M, Mashohor S. Review of brain MRI image segmentation methods. *Artificial Intelligence Review* 2010; **33**:261–274.
3. Atkins MS, Mackiewich B, Whittall K. Fully automatic segmentation of the brain in MRI. *IEEE Trensaction on Medical Imaging* 1998; **1**(17):98–107.
4. Khotanlou H, Colliot O, Atif J, Bloch I. 3D brain tumor segmentation in MRI using fuzzy classification, symmetry analysis and spatially constrained deformable models. *Fuzzy Sets System* 2009; **160**:1457–1473.

5. Cointepas Y, Mangin JF, Garnero L, Poline JB, Benali H. Brain VISA: software platform for visualization and analysis of multi-modality brain data. *Neuroimage* 2001; **6**:339–349.
6. Smith SM. Fast robust automated brain extraction. *Human Brain Mapping* 2002; **17**(3):143–155.
7. Shattuck DW, Leahy RM. Brainsuite: an automated cortical surface identification tool. *Medical Image Analysis* 2002; **6**(2):129–142. DOI: 10.1016/S1361-8415(02)00054-3.
8. Suzuki H, Toriwaki J. Automatic segmentation of head MRI images by knowledge guided thresholding. *Computerized Medical Imaging and Graphics* 1991; **15**(4):233–240.
9. Li C, Godlgof DB, Hall LO. Knowledge-based classification and tissue labeling of MR images of human brain. *IEEE Transaction on Medical Imaging* 1993; **12**:740–750.
10. Aboutanos GB, Dawant BM. Automatic brain segmentation and validation: image-based versus atlas-based deformable models. *Proceedings of the SPIE-Medical Imaging 1997* 1997; **3034**:299–310.
11. Brummer ME, Mersereau RM, Eisner RL, Lewine RRJ. Automatic detection of brain contours in MRI data sets. *IEEE Transaction on Medical Imaging* 1993; **12**:153–166.
12. Cline H, Lorensen W, Kikinis R, Jolesz F. Three-dimensional segmentation of MR images of the head using probability and connectivity. *Journal of Assisted Computer Tomography* 1990; **14**(6):1037–1045.
13. Pannizzo F, Stallmeyer MJB, Friedman J, Jennis RJ, Zabriskie J, Plank C, Zimmerman R, Whalen JP, Cahill PT. Quantitative MRI studies for assessment of multiple sclerosis. *Magnetic Resonance in Medicine*; **24**(1):90–99.
14. Bezdek JC, Hall LO, Clarke LP. Review of MR image segmentation techniques using pattern recognition. *Medical Physic* 1993; **20**(4):1033–1048.
15. Clarke L, Velthuizen R, Phuphanich S, Schellenberg J, Arrington J, Silbiger M. MRI: stability of three supervised segmentation techniques. *Magnetic Resonance Imaging* 1993; **11**(1):95–106.
16. Song T, Jamshidi M, Lee R, Huang M. A modified probabilistic neural network for partial volume segmentation in brain MR image. *IEEE Transactions on Neural Networks* 2007; **18**(5):1424–1432. DOI: 10.1109/TNN.2007.891635.
17. Mitchell JR, Karlik SJ, Lee DH, Fenster A. Computer-assisted identification and quantification of multiple sclerosis lesions in MR imaging volumes in the brain. *Journal of Magnetic Resonance Imaging*; **4**(2):197–208.
18. Chang PL, Teng WG. Exploiting the self-organizing map for medical image segmentation. *IEEE Symposium on Computer-Based Medical Systems* 2007; **0**:281–288.
19. Gerig G, Martin J, Kikinis R, Kubler O, Shenton M, Jolesz FA. Unsupervised tissue type segmentation of 3D dual-echo MR head data. *Image Vision Comput* 1992; **10**:349–360.
20. Zhang DQ, Chen SC. A novel kernelized fuzzy c-means algorithm with application in medical image segmentation. *Artificial Intelligence in Medicine* 2004; **32**(1):37–50.
21. Hall L, Bensaid A, Clarke L, Velthuizen R, Silbiger M, Bezdek J. A comparison of neural network and fuzzy clustering techniques in segmenting magnetic resonance images of the brain. *IEEE Transactions on Neural Networks* 1992; **3**(5):672–682. DOI: 10.1109/72.159057.
22. Tian D, Fan L. A brain MR images segmentation method based on SOM neural network. *The 1st International Conference on Bioinformatics and Biomedical Engineering, ICBBE 2007*, 2007; 686–689.
23. Bomans M, Hohne KH, Tiede U, Riemer M. 3D segmentation of MR images of the head for 3D display. *IEEE Transactions on Medical Imaging* 1990; **9**(2):177–183. DOI: 10.1109/42.56342.
24. Dellepiane S. Image segmentation: errors, sensitivity, and uncertainty. *Engineering in Medicine and Biology Society, Proceedings of the Annual International Conference of the IEEE* 1991; **13**:253–254. DOI: 10.1109/IEMBS.1991.683923.
25. Bankman IN. *Handbook of Medical Image Processing and Analysis*. Academic press, 2008.
26. Snell JW, Merickel MB, Ortega JM, Goble JC, Brookeman JR, Kassell NF. Segmentation of the brain from 3D MRI using a hierarchical active surface template. *In Proceedings of the SPIE Conference on Medical Imaging. SPIE*, San Diego, California, 1994; 2–9.
27. Kass M, Witkin A, Terzopoulos D. Snakes: active contour models. *International Journal of Computer Vision* 1988; **1**:321–331.
28. Lundervold A, Storvik G. Segmentation of brain parenchyma and cerebrospinal fluid in multispectral magnetic resonance images. *IEEE Transactions on Medical Imaging* 1995; **14**:339–349.
29. Waks A, Tretiak OJ. Recognition of regions in brain sections. *Computerized Medical Imaging and Graphics* 1990; **14**(5):341–352. DOI: 10.1016/0895-6111(90)90108-N.
30. Martelli A. Edge detection using heuristic search methods. *Computer Graphics and Image Processing* 1972; **1**(2):169–182. DOI: 10.1016/S0146-664X(72)80013-3.
31. Montanari U. On the optimal detection of curves in noisy pictures. *Communications of the ACM* 1971; **14**:335–345.
32. Thedens D, Skorton D, Fleagle S. Methods of graph searching for border detection in image sequences with applications to cardiac magnetic resonance imaging. *IEEE Transaction on Medical Imaging* 1995; **14**:42–55.
33. Olszewski ME, Wahle A, Mitchell SC, Sonka M. Segmentation of intravascular ultrasound images: a machine learning approach mimicking human vision. *International Congress Series* 2004; **1268**:1045–1049. DOI: 10.1016/j.ics.2004.03.252. CARS 2004 - Computer Assisted Radiology and Surgery. Proceedings of the 18th International Congress and Exhibition.
34. Sonka M, Winniford M, Collins S. Robust simultaneous detection of coronary borders in complex images. *IEEE Transactions on Medical Imaging* 1995; **14**(1):151–161. DOI: 10.1109/42.370412.
35. Falcao A, Udupa J, Miyazawa F. An ultra-fast user-steered image segmentation paradigm: live wire on the fly. *IEEE Transactions on Medical Imaging* 2000; **19**(1):55–62. DOI: 10.1109/42.832960.

36. Sonka M, Hlavac V, Boyle R. *Image Processing, Analysis and Machine Vision* (3rd edn). Chapman and Hall: London, 1993.
37. Dincic M, Peric Z, Jovanovic A. Optimal polar image sampling. *Opto-Electronics Review*; **19**:249–255.
38. David BL, Bong KHL. Application of fixed-radius Hough transform in eye detection. *International Journal of Intelligent Information Technology Application* 2009; **2**:121–127.
39. Gao J, Zhang S, Lu W. Application of Hough transform in eye tracking and targeting. *9th International Conference on Electronic Measurement Instruments, ICEMI 2009*, Beijing, 2009; 3–751–3–754, DOI: 10.1109/ICEMI.2009.5274208.
40. Ballard DH. Readings in computer vision: issues, problems, principles, and paradigms. Chap. Generalizing the Hough transform to detect arbitrary shapes 1987:714–725.
41. Jaccard P. The distribution of the flora in the alpine zone. *New Phytologist* 1912; **11**(2):37–50.
42. Olson DD, David L. *Advanced Data Mining Techniques* (1st edn). Springer, 2008.